RESOLUTION OF THE 180° AMBIGUITY FOR INVERSE HORIZONTAL MAGNETIC FIELD CONFIGURATIONS

JING LI

Institute for Astronomy, University of Hawaii, Honolulu, HI; jing@ifa.hawaii.edu

TAHAR AMARI

Centre de Physique Théorique de l'Ecole Polytechnique, Palaiseau, France; amari@cpht.polytechnique.fr

AND

YUHONG FAN

High Altitude Observatory, National Center for Atmospheric Research, Boulder, CO; yfan@hao.ucar.edu

ABSTRACT

A well-known problem in solar physics is that solutions for the transverse magnetic field direction are ambiguous with respect to a 180° reversal in the field direction. In this paper we focus on three methods for the removal of the 180° ambiguity applied to three MHD models. These methods are (1) the reference field method, (2) the method of magnetic pressure gradient, and (3) the magnetic field divergence-free method. All three methods are noniterative, and methods 2 and 3 are analytical and fast. We apply these methods to three MHD equilibrium model fields: (1) an analytical solution of a nonlinear force-free magnetic field equilibrium from Low, (2) a simulation of an emerging twisted flux tube from Fan & Gibson, and (3) a pre-eruptive twisted magnetic flux rope equilibrium reached by relaxation from Amari et al. We measure the success of methods within "inverse horizontal field" regions in the boundary, which are mathematically defined by $\boldsymbol{B}_\perp \cdot \nabla_\perp B_z > 0$. When such regions overlap with the magnetic field neutral lines, they are known as "bald patches" (BPs) or inverse topology. Our most important conclusion is that the magnetic divergence-free method is far more successful than the other two methods within BPs. This method requires a second level of measurements of the vertical magnetic field. As high-quality multilevel magnetograms will come online in the near future, our work shows that multilayer magnetic field measurements will be highly desirable to objectively and successfully tackle the 180° ambiguity problem.

Subject headings: MHD — Sun: magnetic fields

Online material: color figures

1. INTRODUCTION

After three decades of effort, photospheric magnetic fields are still the most accessible observational data concerning magnetic fields in the solar atmosphere. They provide crucial information on understanding magnetic fields even at other levels where the field cannot be easily determined. As much as we depend on the photospheric magnetic field measurements, the 180° ambiguity remains a problem that inhibits the effective use of vector magnetic fields taken in the photosphere. The problem occurs because all common magnetographs exploit the Zeeman effect (Hagyard et al. 1982; Mickey 1985; Ai & Hu 1986; Lites et al. 1993; Sakurai et al. 1995; Mickey et al. 1996). A spectrum line is split and polarized when a magnetic field is present. Vector magnetic fields are inferred from circular and linear polarization often represented by the Stokes parameters, *I*, *Q*, *U*, and *V*. As the transverse magnetic field directions are invariant to linear polarization states, this inherently results in two possible values differing by 180° in the direction of the transverse magnetic fields (Unno 1956). In a nutshell, the problem is that the observed transverse field has an azimuth angle γ or $\gamma + 180°$, and we cannot easily tell which direction is correct.

Numerous efforts have been made toward solving the 180° ambiguity problem (Amari & Démoulin 1992). Methods have evolved gradually from a simple comparison between observed and extrapolated fields to computerized automatic procedures. These methods can be classified as "reference field" (Gary & Hagyard 1990), "multistep process" (Canfield et al. 1993; Wang et al. 2001; Moon et al. 2003), "interactive," such as the AZAM utility implemented by B. Lites (Metcalf et al. 2006), "automated minimization" (Metcalf 1994; Georgoulis et al. 2004), "vertical current minimization" (Gary & Démoulin 1995; Georgoulis 2005), "noniterative analytical" (Cuperman et al. 1993; Li et al. 1993; Skumanich & Semel 1996), and "spectroscopic" (Landi Degl'Innocenti 1993). Except for the spectroscopic method and the noniterative analytical methods by Cuperman et al. (1993) and Li et al. (1993) that were tested with a MHD model, all the other methods are routinely applied to observational data by individual researchers. Recently, Metcalf et al. (2006) provided an overview of nearly all existing algorithms for resolving the 180° ambiguity problem when applied to synthetic data at a single height level. They concluded that the minimization method is the most promising, but it is time consuming.

Our approach is to compare three methods: the reference field method, the magnetic pressure gradient method, and the magnetic field divergence-free method, as applied to three MHD models. Among these methods, the reference field method is the most commonly used and easily implemented in observations. The magnetic pressure gradient method is based solely on the force-free magnetic field assumption. The divergence-free method is based on the universal rule of the magnetic field, which is free of divergence everywhere. This condition requires a second level of magnetic field, which forms a major obstacle to a broad use of the method for solving the 180° ambiguity problem. It has only been explored by a few in the literature (Li et al. 1993; Boulmezaoud & Amari 1999) with an analytic nonlinear force-free field model (Low 1982), but has never been used solely on real observations.

The three methods are examined by Cuperman et al. (1992, 1993) and Li et al. (1993) using Low's solution. The second and the third methods are not iterative. They solve the $180°$ ambiguity problem 1 pixel at a time. In the current work we apply the three methods to the Low model and two other MHD models. We configure the Low model to a different quadruple-like configuration in the photosphere from those used by Cuperman et al. (1992, 1993) and Li et al. (1993). It resembles some flare-productive regions as determined from observations and simulations (Antiochos et al. 1999; Li et al. 2005).

On physical grounds, it is well known that photospheric magnetic fields are not force-free, because they are in a high-β environment where both neutral and ionized gas pressure balance with magnetic pressure (Metcalf et al. 1995). Most importantly, the instability of the magnetic field leading to solar flares and coronal mass ejections probably originates in the corona, where the field constantly adjusts to equilibrium as a result of continuous plasma motions in the boundary. This picture is reflected by the recent progress on three-dimensional simulations of large-scale magnetic flux eruptions (Amari et al. 2000, 2003a, 2003b, 2004, 2005, 2006; Fan & Gibson 2003, 2004; Leka et al. 2005). Instead of solving MHD equilibrium equations with the photospheric field as a boundary condition, these models follow the evolution of a coronal magnetic configuration that is driven by photospheric or subphotospheric constraints. In two particular models of interest in this paper, the instability is caused either by a twisted flux tube rising at constant speed from the boundary to the corona (Fan & Gibson 2004) or by some photospheric constraints associated with flux cancellation or diffusion (Amari et al. 2000). Both simulations consider rising flux tubes interacting with either a surrounding, nearly potential magnetic field in the corona or a totally unconfined configuration. Differing from Low's model, both simulations describe the dynamic status of the magnetic field from the boundary to the corona. It is compelling to examine whether the three methods used to remove the $180°$ ambiguity problem will succeed over a majority of pixels in the dynamic simulations as they did with Low's force-free field analytic solution. In order to effectively compare the success of the methods, the success rates are estimated within a mathematically defined magnetic field configuration called the "inverse horizontal field." The configurations imply the presence of twisted flux ropes over magnetic polarity inversion lines in both the Fan and Amari models, but not in the Low model.

We organize our presentation as follows. In § 2 we describe the three MHD models and discuss their differences. In § 3 we introduce the three methods used to remove the $180°$ ambiguity problem. In § 4 we explain the experiment procedure. Section 5 provides the test results and discussions. A summary is given in § 6.

2. MODELS

All three models that we use to test the $180°$ ambiguity methods are current-carrying bipolar configurations in the boundary. Among the models of Low (1982), Fan & Gibson (2003, 2004), and Amari et al. (2000), the Low model is a strict nonlinear force-free solution, while the Fan and Amari models are not force-free in the boundary. A significant difference between the models is the distribution of the inverse horizontal field configuration, i.e., the horizontal field pointing in the direction of positive polarity or the direction of increasing vertical field. Mathematically, this can be expressed as $\boldsymbol{B}_\perp \cdot \nabla_\perp B_z > 0$. When this condition occurs over the vertical magnetic polarity inversion line, it is called "inverse topology" by Low & Hundhausen (1995), who described magnetic support of the quiescent filaments. It is also called a "bald patch" (BP) by Titov & Démoulin (1999), which describes

where coronal field lines touch the boundary and return to the corona.

2.1. Model 1: An Analytical Nonlinear Force-Free Field

Low (1982) proposed an analytic nonlinear force-free magnetic field model. The model derivation is carried out in spherical polar coordinates, (r, θ, φ), and is expressed in Cartesian coordinates, (x, y, z). The two coordinates are related, as the origin of the spherical polar coordinates is located at $(0, 0, -a)$, and the polar axis merges with the z-axis in the Cartesian system. An initial potential magnetic field is generated by a straight infinite electric current underneath the photosphere at a given distance, $z = -a$. The magnetic field is axially symmetric about the polar axis during flux emergence. Under the spherical polar coordinates, the force-free magnetic field can be reduced to a scalar nonlinear equation. Under a special case, the magnetic field can be expressed as a function of radial distance r. Transforming the field from spherical polar to Cartesian coordinates, the field components at height z are

$$B_x = -\frac{B_0 a}{r} \cos \varphi(r),$$

$$B_y = \frac{B_0 a x y}{r\left[y^2 + (z+a)^2\right]} \cos \varphi(r) - \frac{B_0 a(z+a)}{y^2 + (z+a)^2} \sin \varphi(r),$$

$$B_z = \frac{B_0 a x(z+a)}{r\left[y^2 + (z+a)^2\right]} \cos \varphi(r) + \frac{B_0 a y}{y^2 + (z+a)^2} \sin \varphi(r), \quad (1)$$

where B_0 is a magnetic field strength constant and $r^2 = x^2 + y^2 + a^2$. The function $\varphi(r)$ is a free generating function related to the force-free field function $\alpha(r)$ by

$$\alpha(r) = -\frac{d\varphi(r)}{dr}. \quad (2)$$

The essence of the model is that the magnetic field vector only varies with latitude θ at a given spherical surface of radius r. "As we move through successive spherical surfaces of increasing r, the vector orientation would vary according to $\varphi(r)$" (Low 1982). The model does not include the time evolution of the field. Various field configurations can be achieved by alternating the generating function, $\varphi(r)$. To test our methods we define a generating function with form $\varphi(r) = (\pi/2) \ln (r/a)$, where $a = 8$ image pixel grids. It produces a magnetic configuration of a quadruple in the photosphere, $z = 0$ (Fig. 1, top). The magnetic topology of the model is like a pair of magnetic flux tubes with opposite polarity twisting together in the boundary. Such twisting is gradually relaxed with increasing height. In Figure 1 (top) the background image is the vertical magnetic field, B_z. The horizontal field vectors are plotted in white and black corresponding to $B_z \leq 0$ and $B_z > 0$, respectively. In the Low model the inverse horizontal field regions do not overlap with the vertical magnetic polarity inversion line, i.e., there is no BP. This is shown in Figure 1 (bottom).

2.2. Model 2: Simulation of a Twisted Flux Tube Emergence

Unlike the analytical nonlinear force-free magnetic field model of Low (1982), Fan & Gibson (2003, 2004) performed three-dimensional numerical simulations of the coronal magnetic field driven by the emergence of a significantly twisted magnetic flux tube. The flux tube emerges into a preexisting coronal arcade that has low plasma β and high electric conductivity. Near the lower boundary where we test the methods, the magnetic fields are non-force-free, but they become force-free very quickly above the
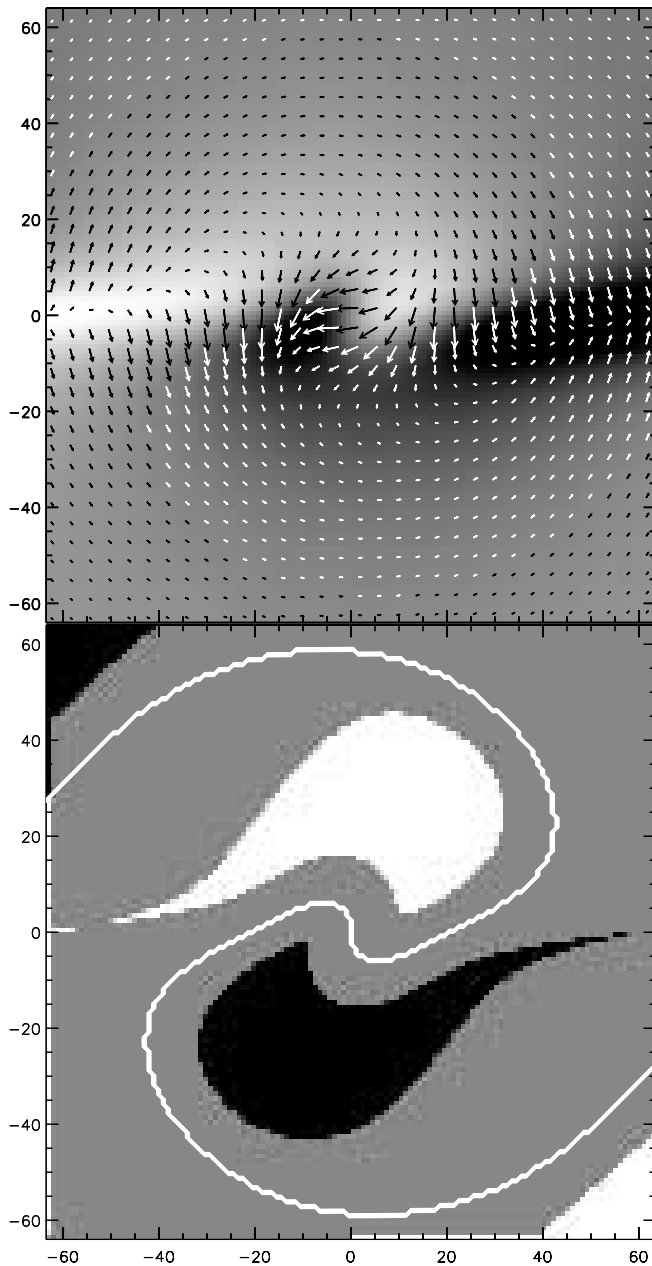
Fig. 1.—*Top*: Nonlinear force-free magnetic field configuration at the photosphere computed from the model by Low (1982). The background image shows the vertical magnetic field with black and white representing opposite polarities. The transverse field vectors are presented by white arrow bars when $B_z \leq 0$ and black arrow bars when $B_z > 0$. *Bottom*: Vertical magnetic polarity inversion line (*solid curve*). White and black patches represent the inverse horizontal field regions corresponding to positive and negative B_z, respectively. [*See the electronic edition of the Journal for a color version of this figure.*]
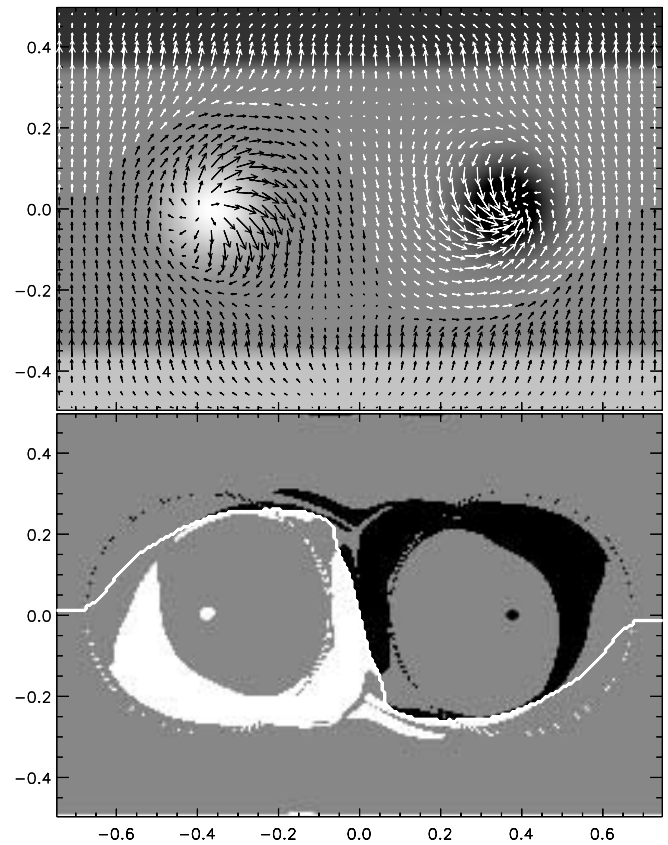

Fig. 2.—*Top*: Magnetic field configuration at the lower boundary in the simulation of twisted flux tube emergence (Fan & Gibson 2003, 2004). The snapshot field is taken at $t = 56$ when the kink instability occurs. The background image and the white and black arrow bars have the same meaning as in Fig. 1. *Bottom*: Inverse horizontal field regions represented by white and black patches. The different colors indicate positive (*white*) and negative (*black*) vertical magnetic field. The B_z neutral line is marked by the thick solid curve. [*See the electronic edition of the Journal for a color version of this figure.*]

instability causes the formation of an inverse-S-shaped current sheet as viewed from above.

Among the series of intermediate field configurations, we choose to test the removal of the 180° ambiguity with the configuration at the last stage. At this stage, the flux tube undergoes a kink instability, implying an eruption. Figure 2 (*top*) shows the magnetic field in the boundary. As in Figure 1, the black and white horizontal vectors represent the horizontal fields against the positive and negative B_z. The inverse horizontal field region overlaps with the vertical magnetic polarity inversion line, i.e., a BP is present. In fact, it is known from Fan's simulation that such a configuration corresponds to a twisted flux tube tangent to the lower boundary (Fig. 2, *bottom*).

2.3. *Model 3: Simulation of Twisted Flux Tube Eruption*

Also recognizing the formation of bright sigmoid coronal structures prior to eruption, Amari et al. (2000) presented a three-dimensional simulation of flux rope eruption. The simulation starts with a current-free magnetic configuration confined in a large computational box (to mimic the open half-space) with equal lengths in three dimensions. Instead of letting a highly twisted flux rope emerge from the lower boundary, the twisting flux tube is established by first applying twisting motion to the opposite polarity pair in the photosphere. A stable numerical force-free equilibrium is reached when the twisting motion stops and the system is allowed to relax. The magnetic configuration displays a highly

boundary (Leka et al. 2005). The simulations show the dynamic response of the corona when a flux tube rises from the lower boundary with time. The study results in some interesting features consistent with observations. For example, the three-dimensional S-shaped electric current layer along the magnetic inversion line is consistent with the bright S-shapes in the corona, the so-called sigmoids, observed in soft X-rays. They often form in active regions prior to coronal mass ejections (Rust & Kumar 1996). When a sufficient amount of twist is transported into the corona, the emerged flux tube undergoes a kink instability. With an emerging tube of left-handed twist (which is preferred for active region flux tubes in the northern hemisphere), the onset of the kink
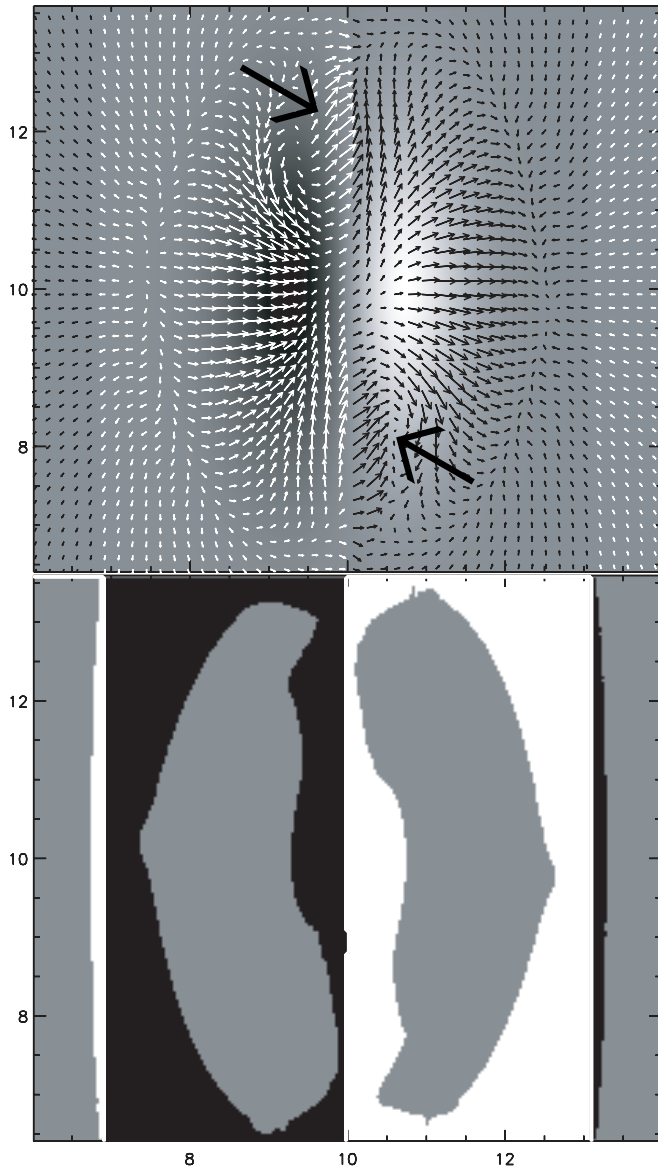
Fig. 3.—*Top*: Two-dimensional magnetic field at the lower boundary from a twisted flux rope eruption model (Amari et al. 2000). The configuration is a snapshot of the field leading to the rapid expansion and reconnection with a higher potential arcade. The background image and the white and black arrow bars have the same meaning as in Fig. 1. Two arrows show the horizontal field vectors pointing away from negative polarity (*upper arrow*) and toward positive polarity (*lower arrow*), forming inverse horizontal field configurations. *Bottom*: Inverse horizontal field regions represented by white (corresponding to $B_z > 0$) and black (corresponding to $B_z \leq 0$) patches. The vertical magnetic polarity inversion lines are overlapped with the rectangle regions outlining the inverse horizontal field regions, making them invisible in the plot. [*See the electronic edition of the Journal for a color version of this figure.*]

sheared structure near the polarity neutral line. To simulate flux cancellation, two opposite polarities start to emerge inside the initial bipolar configuration, reducing the total signed magnetic flux. When a critical amount of flux cancellation is reached, the magnetic topology of the configuration changes from arcadelike to flux-rope-like, exhibiting a twisted flux rope in equilibrium. Then further cancellation leads to the global disruption of the flux rope.

This simulation uses a different driving mechanism at the lower boundary from that of the emergence of a twisted flux tube (Fan & Gibson 2003). The magnetic field twisting is generated by rotating motions of the polarity pair in the boundary. The flux rope is only

formed from an arcadelike structure after an opposite polarity pair emerges within the original polarity pair and a critical magnetic flux cancellation is reached. Figure 3 (*top*) shows the Amari model in the boundary. The configuration is a snapshot of the simulation at equilibrium, which later leads to rapid expansion and reconnection. The latter occurs between the expanded field lines and the overlaying potential field lines.

It is like the Fan model, but unlike the Low model; the electric current density forms a typical sigmoidal shape above the magnetic polarity inversion line as the result of the magnetic reconnections when the critical magnetic cancellation is reached. The horizontal field vectors visibly point away from the negative and toward the positive polarities at the sites where the emerging polarity pair appears (see the two big arrows in Fig. 3, *top*). This corresponds to the twisted flux tube tangent to the lower boundary, and the BP is present (see Fig. 3, *bottom*). The vertical magnetic polarity inversion lines overlap with the rectangle shape of the inverse horizontal field regions. As a result, they are not easily identified in the plot.

3. METHODS

In this section we describe how the three methods are implemented to solve the 180° ambiguity problem in the transverse fields with models.

3.1. *Method 1: Reference Field Method*

This method is the most commonly used for solving the 180° ambiguity problem (Gary & Hagyard 1990). In the current work, the directions of the transverse field, $\boldsymbol{B}_\perp$, are determined by comparing them with the potential transverse field directions, $\boldsymbol{B}_{\perp,\mathrm{pot}}$. The potential fields are calculated using a Green's function with the line-of-sight longitudinal field as a boundary condition (Chiu & Hilton 1977). The field directions are chosen such that the angles between transverse fields and potential fields are less than or equal to 90°, i.e., $\boldsymbol{B}_\perp \cdot \boldsymbol{B}_{\perp,\mathrm{pot}} \geq 0$. This implies that the reference potential field method assumes that the field behaves like a potential field. This method can easily fail in locations where the fields are nonpotential.

3.2. *Method 2: Magnetic Field Pressure Gradient*

An analytic method is developed by the condition that the magnetic field is nonlinear and force-free (Cuperman et al. 1993). Under this assumption, magnetic fields are proportional or parallel to the electric current density,

$$\nabla \times \boldsymbol{B} = \alpha \boldsymbol{B}, \qquad (3)$$

where α is a scalar varying with space and time. We take the cross product of the above equation and $\boldsymbol{B}$ to obtain

$$\boldsymbol{B} \times (\nabla \times \boldsymbol{B}) = 0. \qquad (4)$$

This is equivalent to

$$\boldsymbol{B} \times (\nabla \times \boldsymbol{B}) = \frac{1}{2}\nabla B^2 - (\boldsymbol{B} \cdot \nabla)\boldsymbol{B}. \qquad (5)$$

Because the left-hand side of the equation is equal to zero, the equation leads to

$$\frac{1}{2}\nabla B^2 = (\boldsymbol{B} \cdot \nabla)\boldsymbol{B}. \qquad (6)$$

In Cartesian coordinates, the z-component of the above equation is

$$\frac{1}{2}\frac{\partial}{\partial z}B^2 = \left(B_x\frac{\partial}{\partial x} + B_y\frac{\partial}{\partial y} + B_z\frac{\partial}{\partial z}\right)B_z. \qquad (7)$$

Combining the above equation with the magnetic field divergence-free condition $\nabla \cdot \boldsymbol{B} \equiv 0$, one obtains

$$\frac{1}{2}\frac{\partial}{\partial z}B^2 = \left(B_x\frac{\partial B_z}{\partial x} + B_y\frac{\partial B_z}{\partial y}\right) - B_z\left(\frac{\partial B_x}{\partial x} + \frac{\partial B_y}{\partial y}\right), \quad (8)$$

where $B^2 = B_x^2 + B_y^2 + B_z^2$. Variables appearing on the right-hand side of the equation are the three observable magnetic components in the photosphere, and the 180° ambiguous directions of B_x and B_y. We assume that the magnetic pressure decreases with vertical direction perpendicular to the solar surface; i.e., the magnetic pressure gradient is negative,

$$\frac{\partial}{\partial z}B^2 \le 0. \qquad (9)$$

This is the heart of method 2; the signs of $\boldsymbol{B}_\perp$ are determined to satisfy the above equation at each pixel with the three observable magnetic field components in the photosphere. It is interesting to point out that the first term of the right-hand side of equation (8) is $\left(B_x\partial B_z/\partial x + B_y\partial B_z/\partial y\right) = \boldsymbol{B}_\perp \cdot \nabla_\perp B_z$. When $\boldsymbol{B}_\perp \cdot \nabla_\perp B_z > 0$, it is the inverse horizontal field as defined in the beginning of § 2. With the condition that $\boldsymbol{B}_\perp \cdot \nabla_\perp B_z \le 0$, Krall et al. (1982) determined the directions of observed transverse fields. It is clear that this condition is not sufficient to describe a BP, the configuration of which indicates the presence of a magnetic flux rope. The second term, $-B_z\left(\partial B_x/\partial x + \partial B_y/\partial y\right) = -B_z(\partial B_z/\partial z)$, is due to the universal magnetic divergence-free condition. In this regard, the method is one step closer than method 1 to representing a realistic solar magnetic field condition. However, the negative magnetic pressure gradient represented by equation (9) is not a natural property of the magnetic field. The method will result in disagreement in regions where B^2 increases with z. We further discuss the success and failure of the method in § 5. It is noted that the relation used in this method is only satisfied when the magnetic field is expressed in heliographic coordinates.

The pixel positions are denoted by (i, j) in the boundary in the heliographic system. We approximate infinite partial differentiations into finite differences between neighboring pixels. The partial differences are written as $\Delta B_v^i = B_v(i + \Delta i, j) - B_v(i, j)$, $\Delta B_v^j = B_v(i, j + \Delta j) - B_v(i, j)$, where B_v represents the magnetic field components when $v = x, y, z$ in the boundary. The right-hand side of equation (8) is discretized with equal grid units in the x- and y-axes, $\Delta i = \Delta j$,

$$P \equiv B_x\left(\Delta B_z^i\right) + B_y\left(\Delta B_z^j\right) - B_z\left(\Delta B_x^i + \Delta B_y^j\right). \quad (10)$$

The method is analytical and noniterative. The right-hand side of equation (10) is calculated at each pixel for given magnetic field components B_x, B_y, and B_z among which B_x and B_y are to be determined for 180° ambiguous directions. In our current work we start with an initial transverse field pointing upward; i.e., the transverse field azimuth with respect to the x-axis, γ, varies from 0° to 180°. At each pixel, if the calculated value satisfies the criterion, i.e., $P \le 0$, the transverse field direction remains the same as the initial state; otherwise, the direction is flipped 180°. Although the calculation of equation (10) involves neighboring pixels,

the transverse field direction is determined only at the current pixel. The same procedure is applied to all pixels throughout the region with the initial transverse field directions without iteration. The advantage is that it is fast.

3.3. *Method 3: Magnetic Field Divergence-Free*

From Maxwell's equation,

$$\nabla \cdot \boldsymbol{B} \equiv 0. \qquad (11)$$

Wu & Ai (1991) proposed an alternative method for the removal of the 180° ambiguity in the azimuth of transverse fields. In comparison with the previous two methods, this method is free from any assumption about the solar magnetic fields. Expanding the equation we obtain

$$\frac{\partial B_x}{\partial x} + \frac{\partial B_y}{\partial y} = -\frac{\partial B_z}{\partial z}. \qquad (12)$$

By multiplying both sides of the equation by $\partial B_z/\partial z$, equation (12) becomes

$$\frac{\partial B_z}{\partial z}\left(\frac{\partial B_x}{\partial x} + \frac{\partial B_y}{\partial y}\right) = -\left(\frac{\partial B_z}{\partial z}\right)^2 \le 0. \qquad (13)$$

The left-hand side of this equation consists of observed magnetic field quantities, which are always less than or equal to 0. This criterion was applied by Li et al. (1993) to 20 different magnetic configurations for which exact analytical expressions were given by Low (1982). Like method 2, it is yet another non-iterative and analytical method; therefore, the 180° ambiguity is solved pixel by pixel, and the execution is fast. The difference is that this method requires an observation of the magnetic field at a higher level. In heliographic coordinates with equal grid units in the x- and y-axes, the criterion is discretized in the boundary for all pixels, $z = 0$:

$$Q \equiv \Delta B_z^k\left(\Delta B_x^i + \Delta B_y^j\right) \le 0. \qquad (14)$$

The discrete variables ΔB_x^i and ΔB_y^j have the same meanings as those used in equation (10). When the observing region is near the disk center, an observation of the vertical magnetic field at a higher level, Δk, is needed in order to complete the operation $\Delta B_z^k = B_z(i, j, \Delta k) - B_z(i, j, 0)$. In our work the magnetic fields at a second level are selected at the same height as the grid unit in the x-y plane, equivalent to $\Delta i \equiv \Delta j \equiv \Delta k$. Observationally, it is still a challenge to measure multilayer magnetic fields, but it is comfortably managed with models.

4. EXPERIMENTS

Because our experiments are carried out with MHD models, we need to complete two tasks before applying methods to simulated observational data: (1) Establish the magnetic field in a selected disk location. This is accomplished by performing coordinate transformation. (2) Establish the initial transverse field directions, which are to be determined for either γ or $\gamma + 180°$. This is accomplished by assigning transverse field directions pointing upward for all pixels for the initial transverse field state. Needless to say, this is consistent with the transverse field directions derived from Stokes parameters.

4.1. *Coordinate Transformation*

All three MHD models are expressed in Cartesian coordinates assuming regions situated at the solar disk center. In order to

MODEL	METHOD	W00°,N00° (%)			W15°,N00° (%)			W30°,N30° (%)		
		M_{inv}	M_{B_z}	M_{total}	M_{inv}	M_{B_z}	M_{total}	M_{inv}	M_{B_z}	M_{total}
Low	1	82.6	90.2	96.2	79.8	88.4	95.3	90.2*	91.3*	86.8*
	2	92.4	95.9*	98.8*	78.4	92.6	87.7	80.3	86.6	80.0
	3	93.7*	94.3	97.7	94.2*	93.0*	96.7*	86.3	78.7	76.1
Fan................................	1	47.6	64.6	72.1	47.2	66.5	73.0	53.6	77.7	78.6
	2	4.2	91.8	75.6	20.7	91.4	74.8	23.6	89.4*	74.0
	3	92.5*	94.1*	98.0*	84.4*	93.1*	93.9*	73.5*	88.5	87.6*
Amari	1	0.4	60.9	34.3	4.3	68.4	35.7	25.1	65.8	41.1
	2	7.4	80.1	50.3	21.7	80.6	53.3	23.1	76.3	50.8
	3	89.6*	96.9*	95.1*	74.8*	92.9*	81.1*	71.7*	87.1*	75.3*

NOTES.—The success rate, M_{inv}, is calculated within the inverse horizontal magnetic region shown in the bottom panels of Figs. 1, 2, and 3; $M_{B_z} = \sum |B_z|_{\mathrm{suc}} / \sum |B_z|$ is the ratio of the absolute vertical magnetic field over the number of success pixels to the total number of pixels; M_{total} is the success rate calculated within the entire model region. Asterisks mark the greatest success for each model, method, and location.

obtain off-center magnetic fields we apply the inverse coordinate transformation matrix from equation (1) of Gary & Hagyard (1990) to the models:

$$
\begin{pmatrix} B_{xm} \\ B_{ym} \\ B_{zm} \end{pmatrix} = \begin{pmatrix} a_{11} & a_{21} & a_{31} \\ a_{12} & a_{22} & a_{32} \\ a_{13} & a_{23} & a_{33} \end{pmatrix} \begin{pmatrix} B_{xh} \\ B_{yh} \\ B_{zh} \end{pmatrix}, \qquad (15)
$$

where B_{xm}, B_{ym}, and B_{zm} are the projected model field components. The component B_{zm} is the line-of-sight field, B_{xm} and B_{ym} are the transverse fields at a given disk location, and B_{xh}, B_{yh}, and B_{zh} are magnetic field components in the heliographic plane given by models. The matrix elements are the same as those in equation (1) by Gary & Hagyard (1990), but the matrix here is the transpose matrix of that provided in the equation. This is the first-degree coordinate transformation, as solar global curvature is not considered. In our experiment we consider three disk locations: W00°,N00°, W15°,N00°, and W30°,N30°. They represent the centers of regions, respectively, at the disk center, 15° from the central meridian on the solar equator, and 30° from the central meridian and 30° north.

4.2. Initial Transverse Field Directions

The observed magnetic field components are established in a disk location by the coordinate transformation procedure described above. The observational components B_{xo}, B_{yo}, and B_{zo} are converted from the model magnetic field vectors B_{xm}, B_{ym}, and B_{zm}, but B_{xo} and B_{yo} are 180° ambiguous. The line-of-sight field remains unchanged, $B_{zo} = B_{zm}$. The strength of the transverse field is the same as the observed transverse fields, $|\boldsymbol{B}_{o\perp}| = (B_{xo}^2 + B_{yo}^2)^{1/2} = (B_{xm}^2 + B_{ym}^2)^{1/2}$, but the transverse field directions are assigned 180° ambiguity in azimuth. This is achieved by having the transverse field azimuth, γ, vary between 0° and 180° for all pixels; i.e., the field directions point upward. The final directions are determined by the 180° ambiguity resolution methods described in § 3.

4.3. Coordinates as a Platform for the Removal of the 180° Ambiguity

For method 1, the transverse field directions are determined in the observing plane. The longitudinal fields are used to extrapolate potential fields. For methods 2 and 3, the criteria are only valid in heliographic space. The three observational components, B_{xo}, B_{yo}, and B_{zo}, are first converted to those, B_{xh}, B_{yh}, and B_{zh}, at the helio-

graphic plane using the forward coordinate transformation matrix (Gary & Hagyard 1990). Keep in mind that the horizontal field components, B_{xh} and B_{yh}, are no longer 180° ambiguous under the off-center situation. Along with B_{zh}, they are functions of B_{xo}, B_{yo}, and B_{zo}, where B_{xo} and B_{yo} are 180° ambiguous. The criteria of methods 2 and 3 are calculated in heliographic coordinates, and the signs of B_{xo} and B_{yo} are determined based on the results of the calculation.

5. RESULTS AND DISCUSSION

We estimate the success rates of the methods within inverse horizontal field regions, as they are distinct parts of the magnetic configurations, sometimes leading to eruption when they are BPs. The success rate is calculated as the ratio of the number of correct pixels to the total number of pixels within the inverse horizontal field regions (see the areas of white and black patches in the bottom panels of Figs. 1, 2, and 3). This metric is expressed as a percentage and is denoted with M_{inv}. The correct pixels are those for which the derived horizontal fields agree in direction with those of the models. Two other metrics are calculated for comparison: (1) M_{total}, the ratio of the number of correct pixels to the total number of pixels over the entire region; and (2) $M_{B_z} = \sum |B_z|_{\mathrm{suc}} / \sum |B_z|$, where $|B_z|_{\mathrm{suc}}$ is the absolute vertical field over the pixels for which the 180° ambiguity is successfully removed. The second metric was first used by Metcalf et al. (2006). The success rates are summarized in Table 1. In order to show the success of particular methods clearly, the highest percents are marked with an asterisk within each category. The measurement of success is always carried out in heliographic coordinates. To demonstrate the success of particular methods, Figures 4, 5, and 6 show vector magnetic fields at three disk locations. Only those transverse field vectors of the "successful pixels" are plotted.

5.1. Success and Failure of Methods

All three methods have a high percentage of success with the nonlinear force-free field model (Low 1982; see Table 1). This is consistent with the earlier work by Cuperman et al. (1992, 1993) and Li et al. (1993), although they used slightly different magnetic configurations. Method 1 fails in a small portion of the inverse horizontal field area due to the fact that a potential field does not usually match with the inverse horizontal fields. As for method 2, it should be 100% successful, since the Low model is a strict nonlinear force-free configuration with the method implicit. Yet, the method fails over some pixels at the boundaries
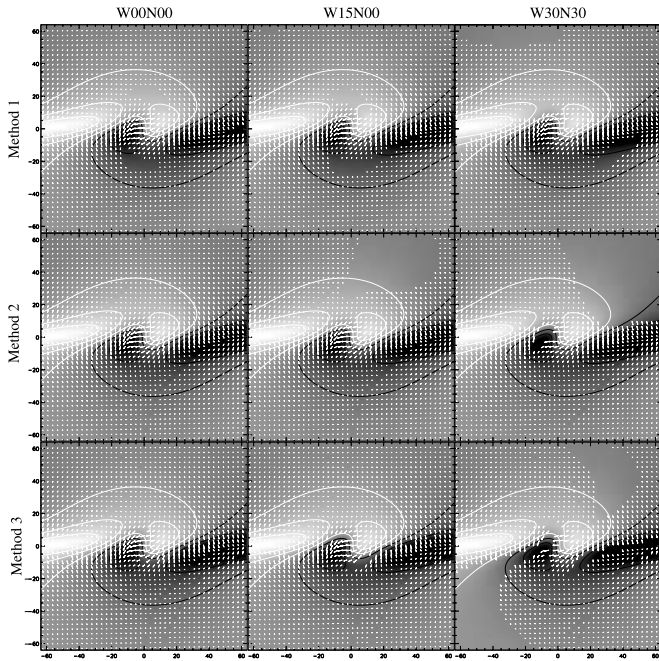
Fig. 4.—Three methods as applied to model 1 (Low 1982) at different disk locations, displayed from left to right. From top to bottom, method 1 is the reference field method, method 2 is the magnetic pressure gradient method, and method 3 is the magnetic divergence-free method. Pixels are plotted where the solutions agree with the original models.

Fig. 6.—Three methods applied to a twisted flux tube eruption simulation (Amari et al. 2000). As in Figs. 4 and 5, pixels are only plotted where the results of the removal of 180° ambiguity agree with the original simulations.

of opposite signs in the 180° ambiguous distribution, B_{xo} and B_{yo} (see the black asterisks in Fig. 7 against the components B_{xo} and B_{yo}). We call this failure the "vicinity-pixel effect," which is near the sudden change in signs of the ambiguous transverse components. This effect also appears in method 3 over the same pixels (see the black asterisks in Fig. 7, *bottom*). A way to eliminate the vicinity-pixel effect was discussed by Boulmezaoud & Amari (1999) when they applied method 3 to Low's model and achieved an almost 100% success rate. They employed a standard interpolation technique that gives weighted contributions from surrounding pixels. The magnetic fields at a given pixel are obtained by integral magnetic fields from surrounding pixels with weighted functions. By minimizing equation (13) over a pixel (x, y), they determine the transverse field signs at the surrounding pixels.
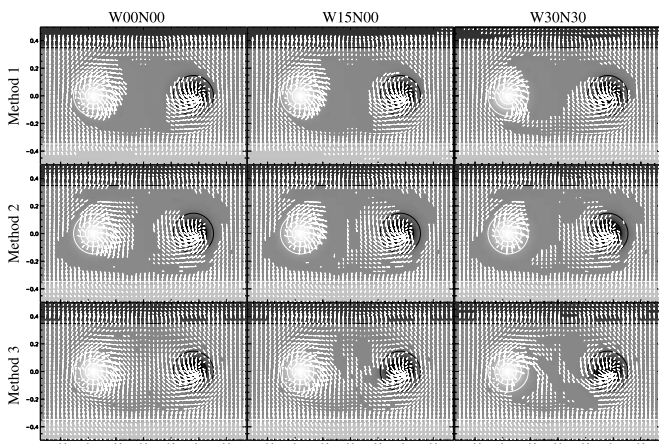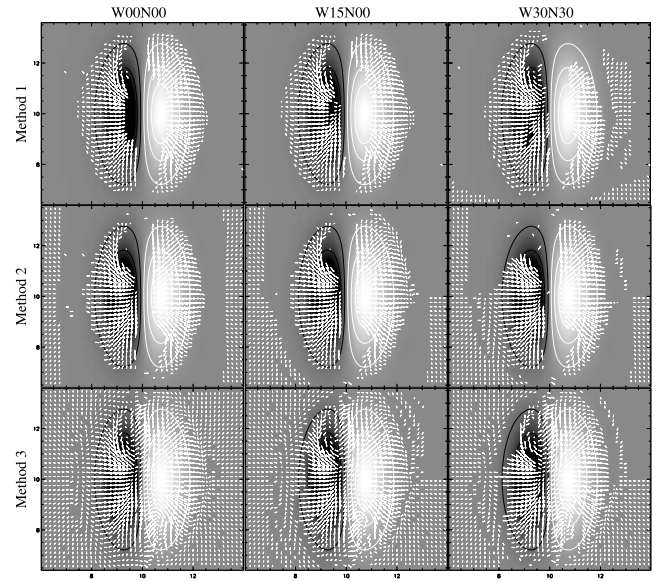

Fig. 5.—Three methods applied to the twisted flux tube emergence model of Fan & Gibson (2003, 2004). Again, the pixels are only plotted with transverse field vectors, where method applications agree with the model.
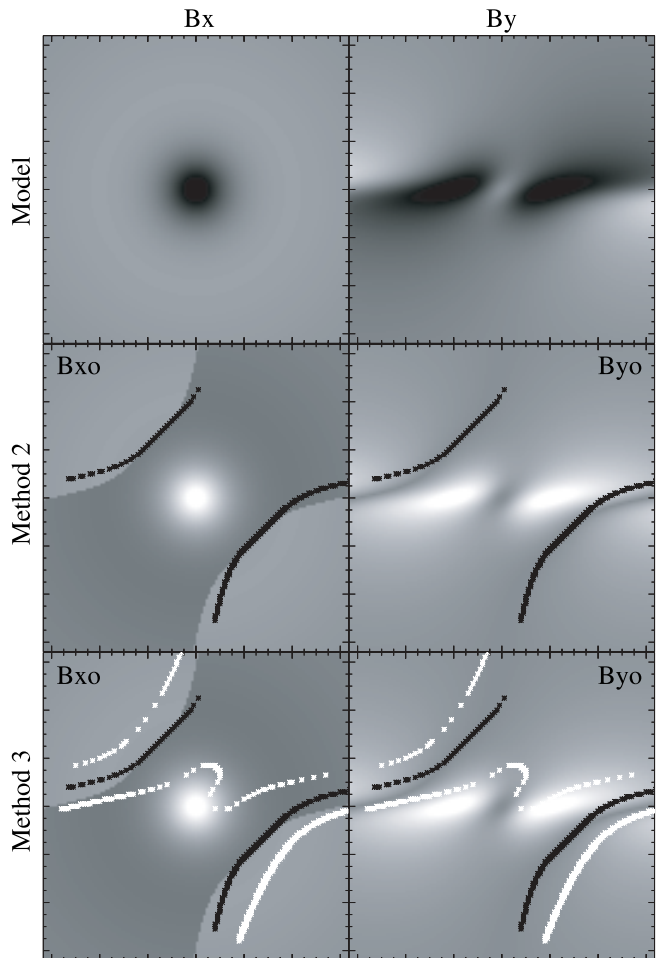

Fig. 7.—Examination of the failure in methods 2 and 3 applied to the Low model field. The true (*top panels*) and ambiguous (*middle and bottom panels*) transverse distributions are displayed here. White areas represent positive values, and the black areas represent negative values of the field strength. Black asterisks mark the pixels where the failure of methods is due to the vicinity-pixel effect (see the text). White asterisks mark the pixels where the method fails due to computational errors when using the criterion of method 3.

Method 1 shows slightly increasing success rates with increasing angular distances for both $M_{\rm inv}$ and M_{B_z}. This is generally true at success rates between disk locations W00°,N00° and W30°,N30° with all models (see $M_{\rm inv}$ with method 1 in Table 1). Since we determine the transverse field directions in an observing plane in method 1, the phenomenon is probably due to the fact that a projected magnetic field is more alike in potential when the region is viewed edge-on. However, this should not be regarded as the common conclusion that method 1 is more successful than other methods when the regions have large angular distances. Indeed, the success rates of method 1 are still low for Fan and Amari models, 53.6% and 25.1%, respectively, within inverse horizontal magnetic field configurations.

Method 1 fails with both Fan and Amari models, as shown in Table 1. The success rates over the entire regions are at 70% and 30% levels for the Fan and Amari models, respectively. But the success rates drop to less than 50% for the Fan model and are only 0%–25% for the Amari model when the pixels are examined within the inverse horizontal field configurations (see also Figs. 5 and 6, *top panels*). Since it is known that both Fan and Amari models contain highly twisted flux tubes over magnetic polarity inversion lines, the failure of method 1 indicates that the extrapolated potential fields are often antiparallel with the real fields within the BP in the boundary.

Method 2 also fails with both Fan and Amari models. The success rates range from a few percent to only 20% within the inverse horizontal field regions. About 85% of the pixels with the Fan model and 17% of the pixels with the Amari model in the inverse horizontal magnetic regions do not satisfy the assumption $\partial B^2/\partial z \le 0$ implicit in method 2 (see the white areas in Fig. 8, *top panels*). Within the inverse horizontal field regions, over 90% of the pixels in both the Fan and Amari models violate the method 2 criterion, equation (10) (see the white areas in Fig. 8, *bottom panels*). The discrepancy between the top and bottom panels in Figure 8 is caused by the non-force-free magnetic fields over pixels, since the right-hand side of equation (8) is only equivalent to equation (9) under the force-free field assumption. The figure suggests that the Amari model departs more from the force-free condition than the Fan model in the boundary, but the Fan model violates $\partial B^2/\partial z \le 0$ more than the Amari model does. As a result, method 2 fails for two reasons with both the Fan and Amari models: (1) the magnetic pressures do not necessarily decrease with height in some pixels, most of which are found in the inverse horizontal field region in the Fan model; and (2) the field distributions are not force-free everywhere, even when magnetic pressures do decrease with height.

Method 3 is the most successful when applied to all three MHD models by all accounts (see Table 1). It is significantly more successful with the magnetic field configurations containing BPs (see the success rates with Fan and Amari models). Some failures occur over small fractions of pixels for two reasons. First, about 1.4% of the pixels in the Low model, 1.6% of the pixels in the Fan model, and 5.0% of the pixels in the Amari model do not satisfy equation (14). As an example, Figure 7 shows pixels marked with white asterisks where $Q > 0$. This was probably caused by the approximate difference calculation between two heights. Second, the rest of the faulty pixels were due to the vicinity-pixel effect, as we described with the Low model in the beginning of this section. The total number of faulty pixels is very small compared with those obtained by methods 1 and 2.

Method 3 requires magnetic field measurements at a second level. When the region is at the disk center, only the vertical field at the second level, $B_{zh}(x, y, \Delta z)$, is needed. When the region is
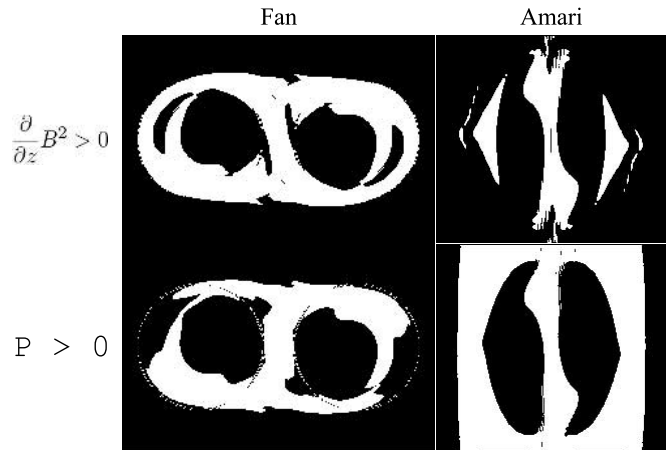

Fig. 8.—Examination of the failure of method 2 applied to MHD simulations by Fan & Gibson (2004) and Amari et al. (2000). *Top panels*: Distributions of $\partial B^2/\partial z$. The distributions are calculated by taking the direct discretized difference between magnetic pressure at two levels: $B^2(x, y, \Delta z) - B^2(x, y, 0)$. White areas represent $\partial B^2/\partial z > 0$, violating a basic assumption of method 2. *Bottom panels*: Distribution of P by eq. (10), where white areas consist of pixels with $P > 0$ violating the criterion of method 2.

off-center, both transverse and line-of-sight components, $B_{xo}(x, y, \Delta z)$, $B_{yo}(x, y, \Delta z)$, and $B_{zo}(x, y, \Delta z)$, are needed at the higher level in order to provide the vertical field, $B_{zh}(x, y, \Delta z)$, through the coordinate transformation procedure. Multilevel magnetic field observations are not yet a common practice among solar observatories, except for a few, such as the Huairou Solar Observatory of the National Astronomical Observatories/Chinese Academy of Sciences,[1] the Mees Solar Observatory,[2] and the National Solar Observatory.[3] The technology to obtain multilevel magnetograms exists, but it is a question of collecting quality data. With high-quality multilevel magnetograms emerging in the near future, method 3 will inevitably become an attractive method, as it does not rely on any assumptions about the magnetic field. Meanwhile, we recognize difficulties with method 3 when it is used on real observational data. The major obstacles with method 3 are as follows: (1) Replacing infinite differentiations with finite numerical difference calculations. Although Boulmezaoud & Amari (1999) proposed a method to deal with this problem, the finite differentials will introduce additional errors by the observational noise. (2) The magnetic field measurements at two levels will have different magnetic sensitivities and spatial resolutions. These problems will have to be dealt with when the method is used on real data.

5.2. *Effect on Current Density and Current Helicity Calculations*

A common application of the photospheric vector magnetic fields is to calculate the electric current density (Lin & Gaizauskas 1987; Canfield et al. 1993; Leka et al. 1993; de la Beaujardiere et al. 1993; Li et al. 1997) and helicity density (Abramenko et al. 1996, 1997; Zhang & Bao 1999). Due to the availability of magnetograms at a single altitude, only the vertical electric current density and the partial electric current helicity are widely calculated. How will the 180° ambiguity resolutions affect electric current density and helicity distributions? With models we examine both full and partial electric current density and current helicity
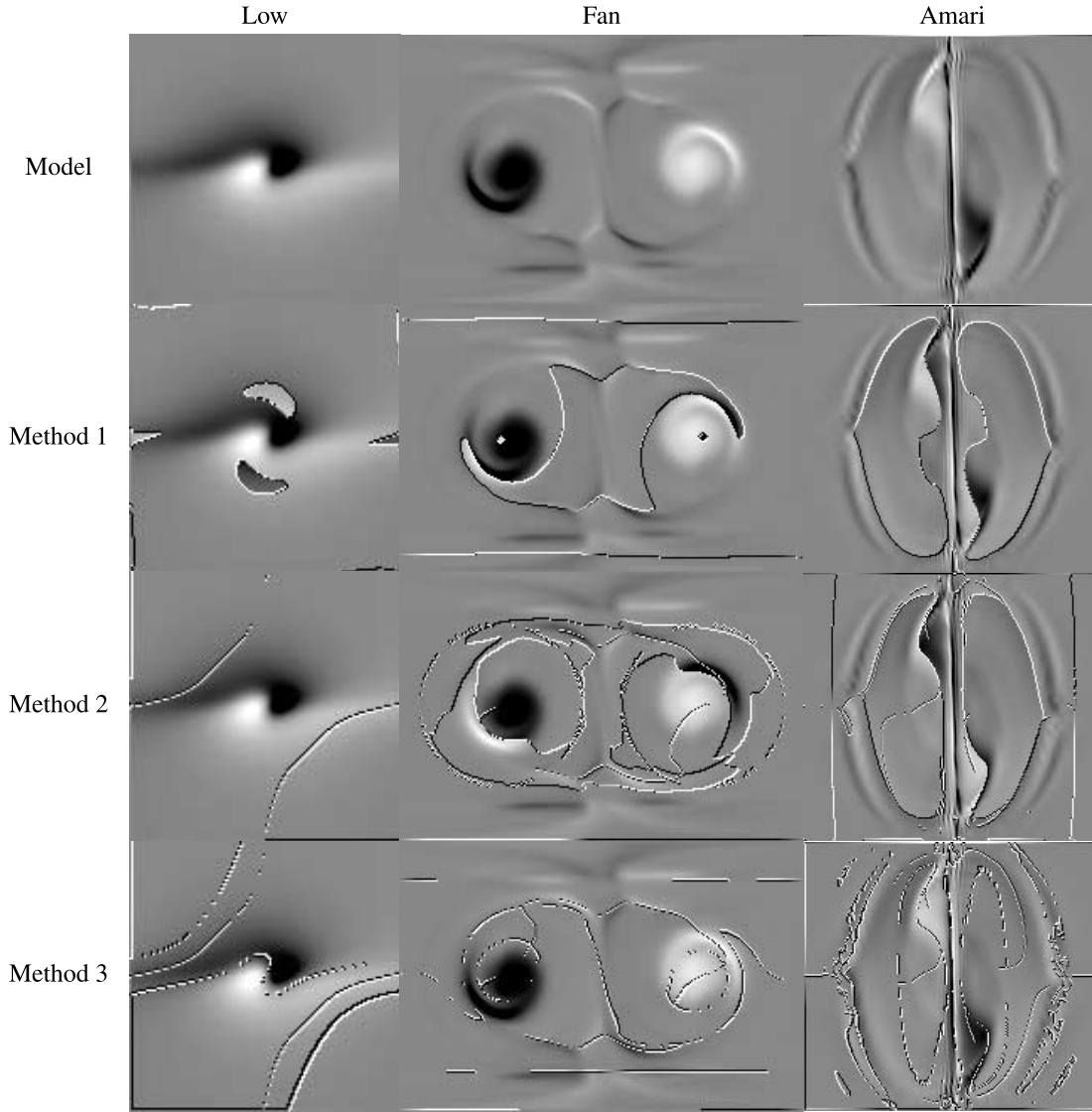
Fig. 9.—Vertical electric current density for the true distributions given by the field models (*top panels*) and the distributions calculated from the fields after the removal of the 180° ambiguity (*middle and bottom panels*). The three columns represent the three models, indicated by "Low" (Low 1982), "Fan" (Fan & Gibson 2004), and "Amari" (Amari et al. 2000).

density. The full electric current density is given by Ampère's law, $\boldsymbol{J} = c/4\pi \nabla \times \boldsymbol{B}$,

$$\frac{4\pi}{c} J_x = \frac{\partial B_z}{\partial y} - \frac{\partial B_y}{\partial z},$$

$$\frac{4\pi}{c} J_y = \frac{\partial B_x}{\partial z} - \frac{\partial B_z}{\partial x},$$

$$\frac{4\pi}{c} J_z = \frac{\partial B_y}{\partial x} - \frac{\partial B_x}{\partial y}, \tag{16}$$

where c is the speed of light. The vertical electric current density J_z is usually calculated using observed photospheric vector magnetic fields (Lin & Gaizauskas 1987; Leka et al. 1993; Wang et al. 1994; Li et al. 1997). In the case of the electric current density, the J_z disagreement between models and the resolved 180° ambiguity fields not only occurs on the "faulty pixels" but also on those surrounding pixels. Therefore, success rates for the electric current density are slightly lower than those for the transverse

fields. Figure 9 shows the vertical electric current density of the "true" distribution (*top panels*), along with the distributions calculated from the resolved 180° ambiguous fields with the three models. As expected, the faulty pixels in which the magnetic field direction is incorrectly computed cause distorted J_z distributions. This is especially evident with the Fan and Amari models using methods 1 and 2. The problematic regions fall on those inverse horizontal magnetic field configurations.

The electric current helicity density is defined as $H_c = \boldsymbol{B} \cdot \nabla \times \boldsymbol{B}$ (Seehafer 1990), i.e.,

$$H_c = B_x \left(\frac{\partial B_z}{\partial y} - \frac{\partial B_y}{\partial z} \right) + B_y \left(\frac{\partial B_x}{\partial z} - \frac{\partial B_z}{\partial x} \right)$$
$$+ B_z \left(\frac{\partial B_y}{\partial x} - \frac{\partial B_x}{\partial y} \right). \tag{17}$$

Figure 10 shows the total current helicity density distribution of the Low, Fan, and Amari models and of the 180° ambiguity–resolved fields in the boundary. With methods 1 and 2, the
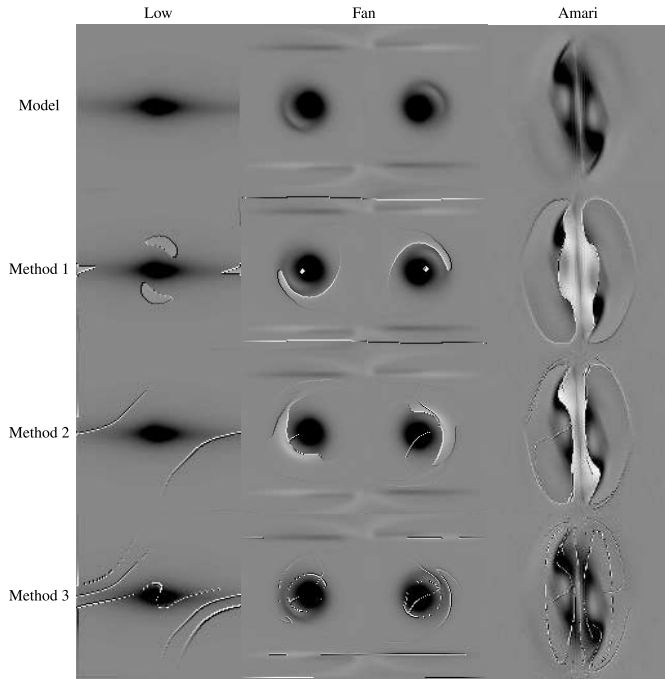
Fig. 10.—Electric current helicity density distribution. The true distributions computed from the magnetic field models are shown on the first row. The density distribution of 180° ambiguity–resolved fields are in the second to fourth rows using methods 1, 2, and 3, respectively. The three columns represent the three models, indicated by "Low" (Low 1982), "Fan" (Fan & Gibson 2004), and "Amari" (Amari et al. 2000).

distributions for the Fan and Amari models have the distributions most distorted from the true ones. This is the same situation as for J_z, namely, that the signs of H_c are reversed mostly within the inverse horizontal field areas. Integrating H_c over the entire region in the boundary, we obtain the surface-integrated electric current helicity $CH = \int H_c\, dx\, dy$. Note that the vertical derivatives of the horizontal fields require the removal of the 180° ambiguity of the transverse fields at the second height. Observationally, the partial surface-integrated current helicity, $pCH = \int B_z(\partial B_y/\partial x - \partial B_x/\partial y)\, dx\, dy$, is usually calculated to represent the electric current helicity of the region from observations (see Abramenko et al. 1996, 1997; Zhang & Bao 1999).

Table 2 lists both the surface-integrated current helicity and partial surface-integrated current helicity over entire regions (the

unit of the current helicity is arbitrary). Their true values are listed in the second and third columns marked "CH" and "pCH," respectively. The helicity values calculated from the resolved 180° ambiguity fields are listed under corresponding disk locations and methods. We mark values of both CH and pCH with asterisks when they approximate the true values. Method 3 gives consistent values that are close to the true values of the three models, especially when the regions are disk-center locations. Comparison between Table 1 and Table 2 shows that the signs of the surface-integrated current helicity are mostly preserved when the number of pixels with the correct sign in the transverse fields is greater than 55%. The total surface-integrated current helicity is insensitive to the "correct transverse field" distribution but sensitive to the total number of "correct pixels."

5.3. Initial State of the Transverse Fields and Success of the Methods

As we have described in § 4.2, we set the initial transverse fields pointing upward throughout the region. In fact, the transverse field azimuth does not exceed 180° after it is derived from Stokes parameters. Therefore, our adoption of the transverse field directions to start with comes directly from observations.

To be general we have tested with initial transverse fields pointing to the right, i.e., γ varies between $-90°$ and $90°$ throughout the region. The successes for the three methods remain exactly the same as when the directions are initially set to vary between $0°$ and $180°$.

A more extreme case is to set the initial transverse field direction randomly to either γ or $\gamma + 180°$ in the individual pixels. This results in directions 180° apart in about 50% of the adjacent pixels throughout the region. The success rate remains unchanged for method 1. This is consistent with the work of method 1, which determines the transverse field directions by comparing fields between observed and extrapolated directions, while the extrapolated field is computed from the longitudinal field. But the success rates are at the 50%–60% level with methods 2 and 3 no matter which MHD model is used, where the region is located on the disk, or whether success rates are calculated within the inverse horizontal field configuration or over the entire region. This is because the randomly assigned transverse field directions depart too far from the true distribution, and the methods are not capable of recovering from too many errors. It is fortunate that such an extreme case violates the magnetic field continuity and is thus not physical. Therefore, such an initial condition is not relevant to our work.

TABLE 2
Full and Partial Surface-integrated Electric Current Helicity

| Model | CH | pCH | Method | W00°,N00° | | W15°,N00° | | W30°,N30° | |
				CH	pCH	CH	pCH	CH	pCH
Low	−1.6e8	−0.6e8	1	−1.6e8*	−0.6e8*	−1.6e8*	−0.6e8*	−1.7e8*	−0.8e8
	−1.6e8	−0.6e8	2	−1.6e8*	−0.6e8*	−1.5e8	−0.6e8*	−0.9e8	−0.6e8*
	−1.6e8	−0.6e8	3	−1.5e8	−0.6e8*	−1.3e8	−0.6e8*	−0.7e8	−0.4e8
Fan.....................	−7.3e4	−3.6e4	1	−6.1e4	−3.1e4	−5.4e4	−3.3e4*	−7.7e4	−6.4e4
	−7.3e4	−3.6e4	2	−4.6e4	−2.2e4	−6.0e4	−4.9e4	−7.2e4*	−5.7e4*
	−7.3e4	−3.6e4	3	−6.7e4*	−3.3e4*	−6.7e4*	−6.0e4	−7.9e4	−8.2e4
Amari	−1.8e3	−0.9e3	1	0.4e3	0.2e3	0.1e3	−0.1e3	0.1e3	0.4e3
	−1.8e3	−0.9e3	2	0.0e3	0.0e3	0.0e3	−0.1e3	−0.4e3	0.2e3
	−1.8e3	−0.9e3	3	−1.6e3*	−0.8e3*	−1.5e3*	−1.2e3*	−1.5e3*	−0.4e3*

Notes.—(CH) Total surface-integrated current helicity within entire model region, eq. (17); (pCH) Partial surface-integrated current helicity calculated with vector magnetic fields in the boundary; $pCH = \int B_z(\partial B_y/\partial x - \partial B_x/\partial y)\, dx\, dy$. Asterisks mark the values closest to the true values (shown in the second and third columns) within each category.

6. SUMMARY

We investigate the resolution of the 180° ambiguity problem in response to the inverse horizontal magnetic field. Three methods are tested with three MHD models. The three methods are the reference field method, force-free field–based magnetic pressure gradient method, and magnetic field divergence-free method. The three MHD models are the nonlinear force-free analytical solution (Low 1982), twisted flux tube emergence model (Fan & Gibson 2004), and flux rope eruption model (Amari et al. 2000). Low's model does not contain BPs, while Fan's and Amari's models do.

1. All three methods are noniterative. Methods 2 and 3 are analytical; i.e., the 180° ambiguity is removed by calculating the criteria pixel by pixel. They are fast in time.

2. Method 1 is not sensitive to the initial transverse field directions, but analytical methods, such as method 2 and especially method 3, are sensitive. They have a high success rate when the initial transverse field directions are set correctly for about 50% of the pixels. In our work, this means the initial transverse fields point upward for all pixels. Methods 2 and 3 are not capable of recovering true fields if the initial transverse field directions are not physical.

3. Although success rates are high with Low's model for all three methods, the actual photospheric magnetic field may not behave as the model describes. For example, the field does not contain a BP. We cannot conclude that all three methods are successful at solving the 180° ambiguity problem based on testing methods with Low's model.

4. The assumptions used in method 1 usually lead to a horizontal field having the property $\boldsymbol{B}_\perp \cdot \nabla_\perp B_z \leq 0$, i.e., a horizontal field pointing in the direction of decreasing B_z. As a result, the method does not work well in resolving the 180° ambiguity for regions satisfying $\boldsymbol{B}_\perp \cdot \nabla_\perp B_z > 0$, especially over the BPs where the inverse horizontal field regions overlap with the vertical magnetic polarity inversion line.

5. Within the inverse horizontal field regions, Fan's model violates the requirement that the magnetic pressure decrease with height more than Amari's model does, while Amari's model is more non-force-free than Fan's model in the boundary. As a result, method 2 fails with both models.

6. Our strongest result is that the magnetic field divergence-free method (method 3) is the most successful in resolving the 180° ambiguity problem for the BPs, which are important for the system eruption. The method depends on magnetic field measurements taken at more than one level. Our experiments strongly indicate that this method is worth the effort to use multilevel magnetic field measurements in order to tackle the 180° ambiguity problem.

7. In methods 2 and 3, the infinite differentiations are replaced with simple numerical differences among neighboring pixels. The current study shows the effect of the nontreated interpixel dependence. Our results demonstrate that the effect is not severe when applying methods to numerical models, especially in the application of method 3.

8. Accuracy of the surface-integrated current helicity depends on the total number of pixels where the signs of transverse fields are correctly determined. The total surface-integrated current helicity is insensitive to the "correct transverse field" distribution but sensitive to the total number of "correct pixels."

9. With method 3, success rates decrease with field locations farther away from the disk center. When the success rates are examined within inverse horizontal magnetic field configurations with method 1, they have a tendency to slightly increase with increasing angular distance of regions. This is probably due to the field distortions, which are more alike in potential when they are viewed edge-on.

While we give a summary of the present experiment above, we are aware that there are some issues that remain to be answered. Issue 1 is that pointing transverse fields upward for all pixels as an initial state is obviously not 100% physical. Although method 3 recovers 98% of the pixels, there may be a more physical initial state in which method 3 will be more successful. Issue 2 is the interpixel dependence implementation. Although the problem is not severe with models, it may become an issue with real observational data with added noise. These two issues are beyond the scope of this paper, and we expect to address them in future work.

REFERENCES

Abramenko, V. I., Wang, T.-J., & Yurchyshyn, V. B. 1996, Sol. Phys., 168, 75
———. 1997, Sol. Phys., 174, 291
Ai, G., & Hu, Y. F. 1986, Publ. Beijing Astron. Obs., 8, 1
Amari, T., Boulmezaoud, T. Z., & Aly, J. 2006, A&A, 446, 691
Amari, T., & Démoulin, P. 1992, in Proc. Méthodes de Détermination des Champs Magnétiques Solaires et Stellaires, ed. E. Landi Degl'Innocenti (Paris: Obs. Paris), 187
Amari, T., Luciani, J., & Aly, J. 2004, ApJ, 615, L165
———. 2005, ApJ, 629, L37
Amari, T., Luciani, J., Aly, J., Mikic, Z., & Linker, J. 2003a, ApJ, 585, 1073
———. 2003b, ApJ, 595, 1231
———. 2000, ApJ, 529, L49
Antiochos, S. K., DeVore, C. R., & Klimchuk, J. A. 1999, ApJ, 510, 485
Boulmezaoud, T. Z., & Amari, T. 1999, A&A, 347, 1005
Canfield, R. C., et al. 1993, ApJ, 411, 362

Chiu, Y. T., & Hilton, H. H. 1977, ApJ, 212, 873
Cuperman, S., Li, J., & Semel, M. 1992, A&A, 265, 296
———. 1993, A&A, 268, 749
de la Beaujardiere, J.-F., Canfield, R. C., & Leka, K. D. 1993, ApJ, 411, 378
Fan, Y., & Gibson, S. E. 2003, ApJ, 589, L105
———. 2004, ApJ, 609, 1123
Gary, G. A., & Démoulin, P. 1995, ApJ, 445, 982
Gary, G. A., & Hagyard, M. J. 1990, Sol. Phys., 126, 21
Georgoulis, M. K. 2005, ApJ, 629, L69
Georgoulis, M. K., LaBonte, B. J., & Metcalf, T. R. 2004, ApJ, 602, 446
Hagyard, M. J., Cumings, N. P., West, E. A., & Smith, J. E. 1982, Sol. Phys., 80, 33
Krall, K. R., Smith, J. B., Jr., Hargvard, M. J., West, E. A., & Cummings, N. P. 1982, Sol. Phys., 79, 59
Landi Degl'Innocenti, E., & Bommier, V. 1993, ApJ, 411, 49

Leka, K. D., Canfield, R. C., McClymont, A. N., de la Beaujardiere, J.-F., Fan, Y., & Tang, F. 1993, ApJ, 411, 370
Leka, K. D., Fan, Y., & Barnes, G. 2005, ApJ, 626, 1091
Li, J., Cuperman, S., & Semel, M. 1993, A&A, 279, 214
Li, J., Metcalf, T. R., Canfield, R. C., Wuelser, J.-P., & Kosugi, T. 1997, ApJ, 482, 490
Li, J., Mickey, D., & LaBonte, B. 2005, ApJ, 620, 1092
Lin, Y., & Gaizauskas, V. 1987, Sol. Phys., 109, 81
Lites, B. W., Elmore, D. F., Seagraves, P., & Skumanich, A. 1993, ApJ, 418, 928
Low, B. C. 1982, Sol. Phys., 77, 43
Low, B. C., & Hundhausen, J. R. 1995, ApJ, 443, 818
Metcalf, T. 1994, Sol. Phys., 155, 235
Metcalf, T. R., Jiao, L., McClymont, A. N., Canfield, R. C., & Uitenbroek, H. 1995, ApJ, 439, 474
Metcalf, T. R., et al. 2006, Sol. Phys., 237, 267

Mickey, D. 1985, Sol. Phys., 97, 223
Mickey, D., Canfield, R. C., Labonte, B. J., Leka, K. D., Waterson, M. F., & Weber, H. M. 1996, Sol. Phys., 168, 229
Moon, Y.-J., Wang, H.-M., Spirock, T.-J., Goode, P. R., & Park, Y. D. 2003, Sol. Phys., 217, 79
Rust, D. M., & Kumar, A. 1996, ApJ, 464, L199
Sakurai, T., et al. 1995, PASJ, 47, 81
Seehafer, N. 1990, Sol. Phys., 125, 219
Skumanich, A., & Semel, M. 1996, Sol. Phys., 164, 291
Titov, V. S., & Démoulin, P. 1999, A&A, 351, 707
Unno, W. 1956, PASJ, 8, 108
Wang, H., Yan, Y., & Sakurai, T. 2001, Sol. Phys., 201, 323
Wang, T. J., Xu, A. A., & Zhang, H. 1994, Sol. Phys., 155, 99
Wu, L., & Ai, G. 1991, Chinese Astron. Astrophys., 15, 240
Zhang, H.-Q., & Bao, S.-D. 1999, ApJ, 519, 876